J Electroceram (2010) 24:122–135
DOI 10.1007/s10832-009-9582-y

Nano-sized $Pr_{0.8}Sr_{0.2}Co_{1-x}Fe_xO_3$ powders prepared by single-step combustion synthesis for solid oxide fuel cell cathodes

Edoardo Magnone · Enrico Traversa · Masaru Miyayama

Received: 18 June 2008 / Accepted: 19 May 2009 / Published online: 4 June 2009

Abstract Different sets of perovskite-type oxides of general formula $Pr_{0.8}Sr_{0.2}Co_{1-x}Fe_xO_{3-\delta}$ (x=0.0, 0.2, 0.5, 0.8 and 1.0) were successfully prepared by low-cost single-step combustion synthesis at low temperatures based on the auto-ignition reaction of a nitrate solution in the presence of citric acid. Thermogravimetric and differential thermal analysis was carried out on nitrate-citrate precursors to determine the perovskite-phase formation process. The results revealed that the nitrate-citrate precursor exhibited self-propagating combustion behavior. $Pr_{0.8}Sr_{0.2}Co_{1-x}Fe_xO_{3-\delta}$ powders showed an orthorhombic single-phase, with their unit cell volume increasing as a function of the Fe content (x). Scanning electron microscopy observations showed that the prepared powders were nanocrystalline. The $Pr_{0.8}Sr_{0.2}Co_{1-x}Fe_xO_{3-\delta}$ powders were characterized as fuel cell electrodes on $Ce_{0.8}Sm_{0.2}O_{2-\delta}$ pellets in symmetrical cells, and the electrochemical properties of the electrode/electrolyte interfaces were investigated using electrochemical impedance spectroscopy (EIS) as a function of the temperature, Fe content (x) and oxygen partial pressure.

Keywords Combustion synthesis · Nanomaterials · Praseodymium · Effect of Fe content · Electrochemical characterization

1 Introduction

Tackling environmental problems is paramount for sustainable development. Energy production using sources alternative to fossil fuels is one of the main problems. Solid oxide fuel cells (SOFCs) are emerging as a green alternative source of energy. Green chemistry is the design of chemical manufacturing systems to minimize their adverse affects on the environment. It is thus paramount to consider green chemistry paradigms for the synthesis process of materials (cathode, electrolyte, and anode) for SOFC production, with the aim to reduce energy consumption and generation of environmentally hazardous-substances.

Despite the recent search for alternative compounds, perovskite-type oxides are still the electrode materials for SOFC cathodes, being $La_{1-x}Sr_xMnO_{3-\delta}$ (LSM) the state-of-the-art compound for high temperature SOFCs and $La_{1-x}Sr_xCo_{1-y}Fe_yO_{3-\delta}$ (LSCF) the best choice for intermediate temperature SOFCs, due to its lower polarization drops [1]. In particular, LSCF possesses high catalytic activity towards the oxygen reduction reaction, high oxygen self-diffusion coefficients, and high electrical conductivity with mixed electronic-ionic conduction that make them suitable as cathode materials for SOFCs at intermediate temperatures [2, 3].

E. Magnone · E. Traversa
NAST Center & Department of Chemical Science and Technology, University of Rome "Tor Vergata",
Via Della Ricerca Scientifica,
00133 Roma, Italy

E. Magnone · M. Miyayama
Research Center for Advanced Science and Technology,
The University of Tokyo,
4-6-1, Komaba, Meguro-ku,
153-8904 Tokyo, Japan

Present address:
E. Magnone (✉)
International Center for Materials Nanoarchitectonics (MANA),
World Premier International (WPI) Research Center,
National Institute for Materials Science (NIMS),
1-1 Namiki,
Tsukuba, Ibaraki 305-0044, Japan
e-mail: MAGNONE.edoardo@nims.go.jp

Several synthesis methods have been developed for SOFC cathode materials and clearly the SOFC electrode performance is correlated with the materials processing [4]. In recent years, combustion synthesis (CS) is becoming one of the most popular methods for the preparation of a wide variety of SOFC materials, ranging from cathode [5] to electrolyte [6] or anode [7].

In a typical scheme, the CS involves the exothermic combustion reaction between an oxidant and an organic fuel as a reductant. Only when the oxidant (such as a metal nitrate) and the fuel (typically citric acid, glycine, urea, etc) are intimately mixed in solution with a fixed proportion, they can initiate an exothermic reaction that generates large amounts of heat [8, 9]. After ignition with an external energy source, the mixture undergoes a rapid exothermic reaction that is normally self-sustaining (also known as "furnaceless synthesis") by the spontaneous generation of heat [10–12]. Among the known fuels, we selected citric acid because of its demonstrated versatility in the field of combustion synthesis [13].

The CS process is simple, fast and energetically economic, and therefore is attracting attention for the preparation of SOFC materials as a low-cost alternative to solid-state reaction processing [14]. The CS main advantages are:

- relatively cheap starting reactants (such as metal nitrates),
- easily available organic molecules as an internal fuel (such as citric acid),
- highly exothermic and self-sustaining reactions (without the addition of an external heat source),
- high energy reaction efficiency (such as a low auto-ignition temperature of synthesis reaction),
- high degree of process repeatability,
- capacity of mass production in a short process time,
- low cost capital of the equipment and low industrialization cost,
- energy-saving synthesis.

For all these reasons, the auto-combustion synthesis method by one-step preparation at moderate temperatures was selected for the preparation of strontium and iron-doped praseodymium cobaltite nano-powders, $Pr_{0.8}Sr_{0.2}Co_{1-x}Fe_xO_{3-\delta}$.

The choice of using Pr as the rare earth element in the perovskite oxide instead of La, studied in a previous paper [15], is due to its peculiarity to show +3 and +4 valence states [16], which might induce interesting electrical properties [17–19].

Kostogloudis and coworkers reported the electrical conductivity of $Pr_{1-x}Sr_xMnO_3$ perovskite-type oxides ($0.0 < x < 0.5$), which have potential use as cathode materials in intermediate-temperature SOFCs because of their p-type electronic conductivity described by the small polaron hopping mechanism [20]. H.-R. Rim et al. reported similar results with calcium and strontium-doped praseodymium manganite powders prepared as cathode materials for SOFC applications [21]. It has been also suggested that the increasing rate of interphase oxygen exchange at either electrode/gas or electrolyte/gas surfaces of praseodymium-containing oxides is determined by their specific electrocatalytic properties, which directly depend on the unusual valence state of praseodymium ions and the formation of oxygen vacancies [22, 23].

There were relatively few reports about $Pr_{1-y}Sr_yCo_{1-x}Fe_xO_{3-\delta}$ system and its properties, especially electrode morphology behavior and electrochemical properties as a function of Sr- and Fe- contents (y and x, respectively). Moreover, regarding electrochemistry behavior, there are poor literature data about $Pr_{0.8}Sr_{0.2}Co_{1-x}Fe_xO_{3-\delta}$ cathode ceramics on its oxygen content (δ) at high temperature or the crystal structure and mechanical properties as a function of Fe content (x). Therefore, in this paper, we will report on the synthesis of nano-sized $Pr_{0.8}Sr_{0.2}Co_{1-x}Fe_xO_{3-\delta}$ (x=0.0, 0.2, 0.5, 0.8 and 1.0) powders by an auto-combustion technique and will discuss the effects of the Fe content (x) on the microstructure of the $Pr_{0.8}Sr_{0.2}Co_{1-x}Fe_xO_{3-\delta}$ electrodes in order to optimize the fabrication process and finally to improve their electrochemical properties. $Pr_{0.8}Sr_{0.2}Co_{1-x}Fe_xO_{3-\delta}$ oxide nanocrystalline powders were characterized as electrodes on $Ce_{0.8}Sm_{0.2}O_{2-\delta}$ pellets in symmetrical cells. The electrochemical properties of the electrode/electrolyte interfaces were investigated using electrochemical impedance spectroscopy (EIS) measurements as a function of the temperature, Fe content (x) and gas atmosphere. This article will describe some of the representative morphologies seen by direct SEM observation of $Pr_{0.8}Sr_{0.2}Co_{1-x}Fe_xO_{3-\delta}$ samples.

2 Experimental

2.1 Precursors

Fine powders of $Pr_{0.8}Sr_{0.2}Co_{1-x}Fe_xO_{3-\delta}$ perovskite compounds (x=0.0, 0.2, 0.5, 0.8, 1.0) were prepared by CS based on the reaction of cations activated by an organic mixture. Praseodymium (III) nitrate hexahydrate (99.99%; Aldrich), strontium (II) nitrate (99+%; Aldrich), cobalt (II) nitrate hexahydrate (98+%, Aldrich), and iron (III) nitrate 9-hydrated (98+%; Aldrich), used as sources of metal cations, were dissolved in pure water. Then, tribasic carboxylic acid, such as citric acid (CA, 2-hydroxypropane-1,2,3-tricarboxylic acid, $C_6H_8O_7$ H_2O, Iso-for analysis, >99.8%, Carlo Erba reagents, CAS: 77-92-9), was used as a chelating agent of metal cations and, straight afterward, as a fuel during combustion. In all experiments the molar ratio

(γ) between fuel (citric acid, CA) and total oxidant (NO_3^-) was set to 1:1, because the energy released by the combustion of the redox mixtures reaches the maximum in heat release rate when the γ ratio is near to unity [8, 24].

2.2 Synthesis and Characterisation of $Pr_{0.8}Sr_{0.2}Co_{1-x}Fe_xO_{3-\delta}$ powders

The aqueous solution containing all metal nitrates and organic fuel was heated at about 393 K for 3 h under stirring in a beaker (Pirex) and a colored gel was obtained. Water vapor gradually evolved with a corresponding increase in viscosity.

The gel was transferred into a ceramic dish and placed into a hot-plate preheated to above 470 K. The gel solution boiled and underwent dehydration followed by a smooth combustion that produced black foam. This foam then was ignited, giving highly voluminous and fluffy black powder combustion products. When ignited at any point, the dried gel burnt in a self-propagating combustion manner until all the gel was completely burnt out to form black soft powders. As-combusted samples were cooled down to room temperature in air. The resulting as-combusted powder was further pulverized by hand grinding in an agate mortar using a pestle, collected and then calcined in static air at 1273 K for 2 h in a muffle furnace. The samples were cooled down to room temperature in the furnace.

To perform thermal analysis, the gel was completely dried in an oven overnight at 373 K. Gas evolutions, in this case, resulted in gel expansion, by which the final volume of the gel became more than three times than the original volume. A soft mass was formed, made of a complex three-dimensional foam-like structure.

The thermal evolution of the dry citric precursor was studied using simultaneous thermogravimetric-differential thermal analysis (TG-DTA), using a Netzsch Analyzer (Model STA 409), on samples of approximately 60 mg, with a heating rate of 5 K/min from room temperature to 1475 K in air flow (100 ml/min), with an α-Al_2O_3 reference.

X-ray diffraction (XRD) analysis was performed to determine the phase identity, crystal structure, and lattice constants of the powders, using a Philips X-ray diffractometer (Model PW-1700, Philips) with CuK_α radiation at 30 kV and 40 mA. XRD data were collected at 2θ angles between 20 and 80° with a step interval of 0.02° at room temperature. Rietveld structure analysis was performed on a powder sample of the $Pr_{0.8}Sr_{0.2}Co_{1-x}Fe_xO_{3-\delta}$ compound. The crystallite size was determined using the Scherrer equation.

Observations of morphology of the as-combusted, calcined powders and electrode films were performed using scanning electron microscopy (SEM, Model S-4500, Hitachi Co, with 4855 Digital Beam Control Interface). Representative micrographs were selected for presentation. The particle size was determined by the intercept line method of SEM observation results.

2.3 Preparation of samples for electrochemical measurements

Dense electrolyte pellets (diameter <1 cm; thickness <0.3 cm) were obtained by ball-milling samaria-doped ceria ($Ce_{0.8}Sm_{0.2}O_{2-\delta}$, SDC) powders, forming the powders by uniaxial pressing, and then sintering at 1873 K for 10 h. The pellet density was estimated to be around 90% of the theoretical density by geometric factors and weight.

The $Pr_{0.8}Sr_{0.2}Co_{1-x}Fe_xO_{3-\delta}$ fine powders were deposited on both symmetrical sides of SDC ceramic pellets ($Pr_{0.8}Sr_{0.2}Co_{1-x}Fe_xO_{3-\delta}$/SDC/$Pr_{0.8}Sr_{0.2}Co_{1-x}Fe_xO_{3-\delta}$, with $0.0 < x < 1.0$) for electrochemical characterization. $Pr_{0.8}Sr_{0.2}Co_{1-x}Fe_xO_{3-\delta}$ powders were mixed with the same volume of polyethyleneglycol and ethyl alcohol and then applied to the electrolyte by painting. The painted pellets were then fired at 1273 K for 1 h in stagnant air. The symmetrical cells thus fabricated were set up in an alumina tube (inner diameter= 2.5 cm).

EIS measurements in the two-electrode configuration were used to characterize the cell electrochemical performance as a function of temperature, Fe content (x) and gas atmosphere. EIS measurements were performed using an in-house-built test station, a Solartron SI 1260 Impedance/Gain-Phase Analyzer and a 1287 Solartron Electrochemical Interface, in the frequency range from 0.01 Hz to 13 MHz (5 points per decade), in the 873 to 1073 K temperature range with a signal amplitude of 10 mV. Pure air or argon was supplied to the symmetrical cell at a continuous flow rate of 30 ml/min during EIS measurements. Gold nets at both sides of the pellets were used as current collectors.

The area-specific resistance (ASR) of the interface and the activation energy (E_a) of each sample were calculated from the EIS data in order to shed some light on the mechanisms of oxygen reduction. ASR values were calculated from the electrode resistance obtained from the difference between the lowest frequency and the highest frequency real-axis intercepts of semicircles in a complex impedance plots.

3 Results and discussion

3.1 Thermal analysis of the citric precursors

The function of CA during the synthesis is two-fold: at first, it acts as a multi-complexing agent for the cations in the nitrate solution; second, it acts as the fuel during the following combustion reactions. It is not our purpose here

to study the formation of the gels in aqueous solution between citric acid and metal nitrates, but only the evolution of the combustion products.

Figure 1 shows the TG and DTA curves of pure $C_6H_8O_7 H_2O$ as a reference and for the $Pr_{0.8}Sr_{0.2}Co_{1-x}Fe_xO_{3-\delta}$ dry citric precursors with x=0.5 and 1, respectively. The TG curve of citric acid (Fig. 1(b)) shows about 90 wt% loss occurring at temperatures between 400 and 650 K, correlated with two DTA endothermic peaks (A- and B -thermal effects in Fig. 1(a)), representing the CA decomposition. Finally, a last minor weight loss (−8 wt%) was observed between 650 and 750 K, associated with a broad and intense DTA exothermic peak centered at 700 K (C-thermal effect). The weight loss behavior is comparable to the trend presented by Mali and Ataie [9]. The C- single exothermal event occurring at about 700 K is ascribable to CA- derivatives by the combustion of any residual citric acid [25–27].

Figure 1(d) and (f) show several weight loss regions for the dry citric precursors corresponding to about 420, 520, and between 600 and 750 K, correlated with D, E and F effects in DTA curves (Fig. 1(c) and (e)), respectively. In the case of the $Pr_{0.8}Sr_{0.2}Co_{0.5}Fe_{0.5}O_{3-\delta}$ citric precursor (x=0.5), the TG curve (Fig. 1(d)) can be divided into three regions: an initial weight loss of 5–10 wt% near 420–430 K, a further weight loss of 30 wt% between 430 and 620 K, and a final weight loss of 10–15 wt% that is nearly completed at 750 K. Moreover, the TG curve (Fig. 1(f)) of the other citric precursor sample (x=1, as the citric precursor without Co ions) can be divided into three regions: after the first weight loss of 10%, a deep weight loss of about 50 wt% for the first heating range up to 500 K and then a final weight loss of 20 wt% between 500 and 750 K that is nearly completed at 800 K.

Each step in the TG curve corresponds to a thermal peak in the DTA curve. A close examination of the DTA curves shows that the first exothermic peak (called D in Fig. 1(c) and (e)) at about 415 K can be related to partial nitrate decomposition. As confirmed by TG analysis, this exothermic reaction at 415 K did not took place for pure CA, where the nitrates were not added (cf. Fig. 1(a)).

The E- and F- thermal effects for the nitrate-citrate precursors observed in the 520–750 K range of the DTA curves (Fig. 1(c) and (e)) can be ascribed to the multi step thermal decomposition of organic compounds and organic acid derivatives (such as aconitic acid, itaconic acid, itaconic anhydride, and acetone-dicarboxylic acid), as also evidenced by the TG curve of pure CA that showed about 85 wt% loss at temperatures between 450 and 650 K. Moreover, a moderate weight loss (approximately 10 wt%

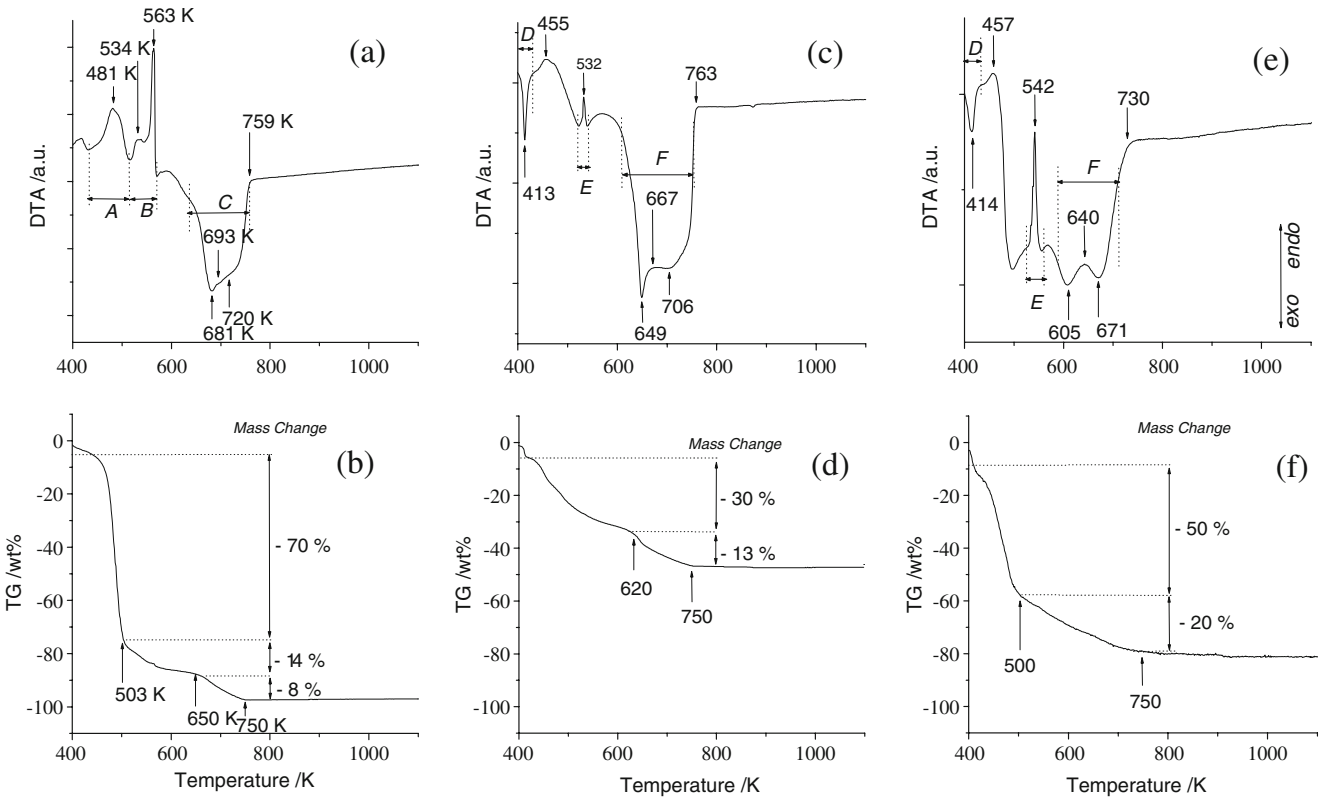

Fig. 1 TG-DTA curves for pure citric acid (**a** and **b**), $Pr_{0.8}Sr_{0.2}Co_{0.5}Fe_{0.5}O_{3-\delta}$ (**c** and **d**) and $Pr_{0.8}Sr_{0.2}FeO_{3-\delta}$ (**e** and **f**) dry citric precursors, obtained with a temperature ramp of 5 K/min from 400 up to 1200 K

of the original weight) of the pure CA sample was observed between 650 and 750 K, which can correspond to the last DTA exothermic peak (C- effect in Fig. 1(a)). It can be concluded that the first nitrate decomposition at relatively low temperature helps combustion of the citric precursor and perovskite-type oxide synthesis.

No further weight loss by TG analysis was observed above approximately 800 K and no endo- or exo-thermal effects were observed above 750 K. It could be assumed that the last weak exothermic effect at about 700 K in DTA curves (F- effect) corresponds also to the synthesis of the $Pr_{0.8}Sr_{0.2}Co_{1-x}Fe_xO_{3-\delta}$ phases.

In summary, for the citric precursors the first small exothermic peak in TG-DTA analysis (D- thermal effect at about 415 K) corresponds to the first nitrate decomposition, the endothermic event at 530–550 K (E- thermal effect) corresponds to the first step of decomposition of organic precursor gels and organic acid derivatives, and the last broad exothermic effect between 600 and 750 K (F–thermal effect) corresponds to the ignition of any residual citric acid, or its derivatives, and formation of perovskite-type oxides.

3.2 Combustion synthesis

When the precursor gel was preheated on a hot plate and kept at a constant temperature of 470 K, the heat released in the fast combustion reaction allowed the formation of the black powders after a few minutes. The combustion was not finished until all the citric precursors were burned out and the resulting product was a black substance which showed voids, pores, and was highly friable, formed by the escaping gases during the combustion reaction. During the CS a large amount of gases are liberated from the citric precursor, and most probably the evolution of gases helped the formation of fine powders by limiting the inter-particle contact and maximizing the solid surface. The reaction was completed before 4 minutes after the start of combustion. All the samples ($0.0<x<1.0$) showed a similar decomposition behavior.

Recently, nanosized catalysts have been synthesized via citrate-nitrate route by hot plate preheated at 430–500 K and the recorded synthesis temperature of initiation of self-propagating flameless combustion front was observed between 670 and 950 K [28, 29]. Our experimental CS results revealed that the citric precursors exhibited self-propagating combustion behavior at low temperatures, and probably the maximum increase in flame temperature was about 200–300 K from ignition temperature of 470 K. Our CS observations were in line with those of literature [8, 24, 27], which further confirm our previous findings by using TG-DTA.

Figure 2(a) and (b) shows the SEM micrographs of the $Pr_{0.8}Sr_{0.2}Co_{0.5}Fe_{0.5}O_{3-\delta}$ ($x=0.5$) and $Pr_{0.8}Sr_{0.2}FeO_{3-\delta}$ ($x=1.0$), respectively. Same morphology was observed for all the as-combusted samples, as a function of Fe content (x).

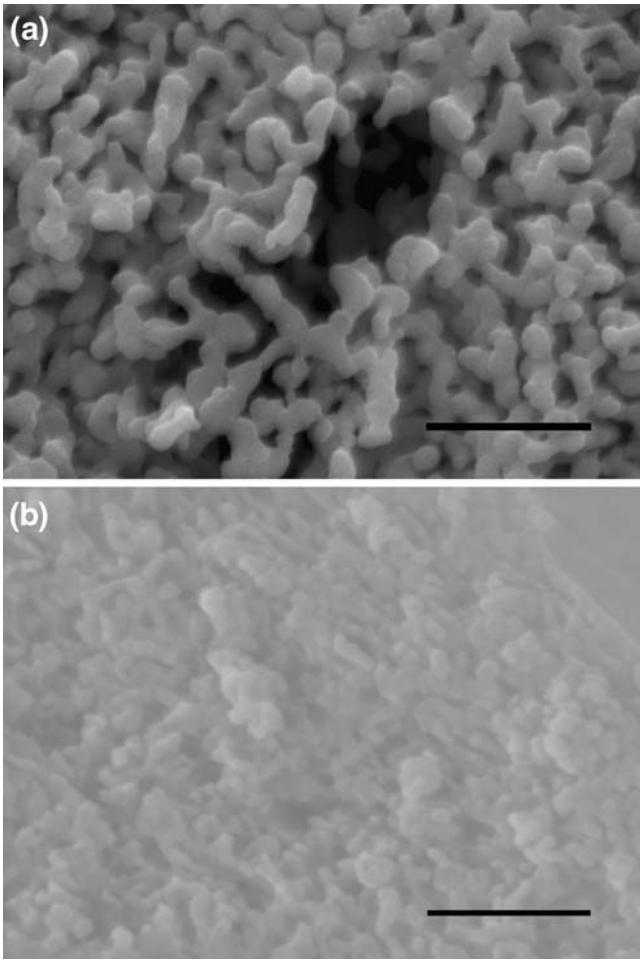

Fig. 2 Representative micrographs of (**a**) $Pr_{0.8}Sr_{0.2}Co_{0.5}Fe_{0.5}O_{3-\delta}$ and (**b**) $Pr_{0.8}Sr_{0.2}FeO_3$-δ as-burnt powders after combustion synthesis (the horizontal black scale marker represents 1.00 μm and 0.30 μm, respectively)

As shown in Fig. 2 the large porous networks were made of randomly-oriented spherical particles. The median grain size of the as-combusted powders measured from the SEM micrographs increased from 40 nm from $Pr_{0.8}Sr_{0.2}FeO_{3-\delta}$ samples to about 150 nm of $Pr_{0.8}Sr_{0.2}Co_{0.5}Fe_{0.5}O_{3-\delta}$, then decreasing again with decreasing the Fe content (x), being 40–60 nm for $Pr_{0.8}Sr_{0.2}CoO_{3-\delta}$. The agglomerates were easily destroyed after milling to produce powders.

3.3 Structural analysis

Figure 3(a) shows the XRD patterns of the powder samples as produced by CS. The appearance of X-ray line broadening indicates the nano-crystallinity of the synthesized powders. Figure 3(b) shows the XRD patterns at room temperature for the powders after thermal treatment at 1273 K. The samples heated to high temperature gave

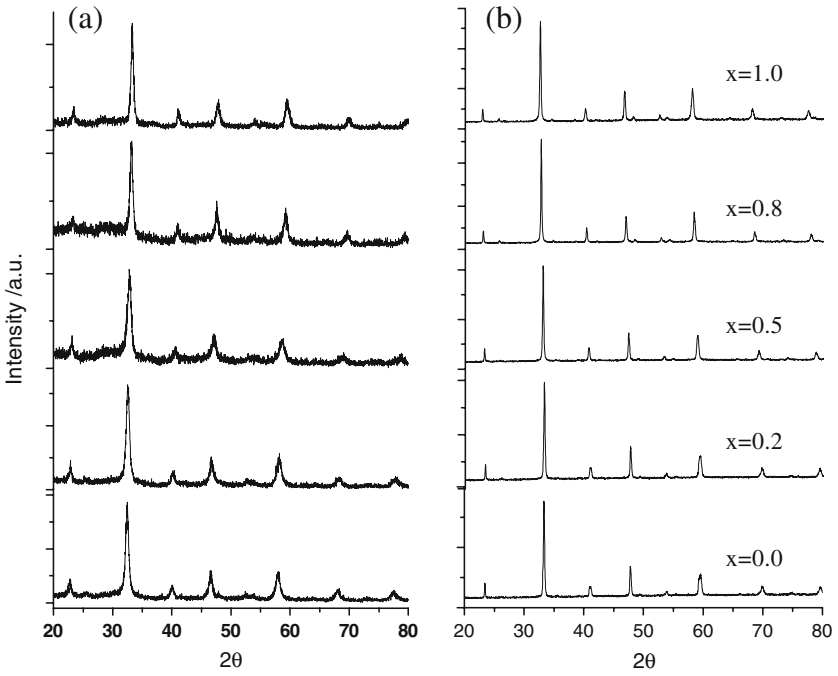

Fig. 3 X-Ray diffraction patterns of (**a**) primary powders obtained by CS of citric precursor and (**b**) calcined powders (1273 K, 2 h)

relatively sharp XRD reflection peaks, indicating the grain growth of oxide crystallites.

All the powders showed single-phase $Pr_{0.8}Sr_{0.2}Co_{1-x}Fe_xO_{3-\delta}$ perovskite-type oxide patterns, but a systematical shift in the peak position towards smaller angles as a function of the Fe content (x) was observed. Since the ionic radius of Fe^{3+} and Co^{3+} are 0.645 Å and 0.61 Å, respectively, the crystal lattice increases with decreasing of the amount of Co^{3+} used to replace the Fe^{3+} position in $Pr_{0.8}Sr_{0.2}Co_{1-x}Fe_xO_{3-\delta}$ perovskite-type oxides. These experimental findings suggest that $Pr_{0.8}Sr_{0.2}CoO_{3-\delta}$ and $Pr_{0.8}Sr_{0.2}FeO_{3-\delta}$ are completely miscible but, objectively, we observed two different peaks splitting (at ~41 and ~59° of 2θ) in the XRD patterns obtained from x=0 and x=0.2 powder samples with low Fe content (x).

It is well know that the crystal symmetry of perovskite-type oxide can change as a function of the stoichiometry of element in metal oxide solid-solution. Also in the present study, for $Pr_{0.8}Sr_{0.2}Co_{1-x}Fe_xO_{3-\delta}$ the perovskite had a distorted orthorhombic structure (Space-group number= 62) was observed for $0.1 \leq x \leq 1.0$ as a function of Fe content (x). The crystal structure of $Pr_{0.8}Sr_{0.2}Co_{1-x}Fe_xO_{3-\delta}$ has been refined by Rietveld profile fitting method (see Table 1).

It has been reported that at room temperature the $LaCo_{1-x}Fe_xO_3$ has a rhombohedral symmetry for $x \leq 0.45$ and orthorhombic symmetry for $x \geq 0.5$, whereas the $La_{0.8}Sr_{0.2}Co_{1-x}Fe_xO_{3-\delta}$ system are rhombohedral and orthorhombic for $x \leq 0.7$ and $x \geq 0.8$, respectively [2]. This suggested that the Sr substitution in the $La_{0.8}Sr_{0.2}Co_{1-x}Fe_xO_{3-\delta}$ solid solution can be extended the region of

Table 1 Structural data for $Pr_{0.8}Sr_{0.2}Co_{1-x}Fe_xO_{3-\delta}$ ($0.0<x<1.0$).

Structural data	Fe content (x)				
	0.0	0.2	0.5	0.8	1.0
a /Å	5.370	5.381	5.425	5.479	5.502
b /Å	5.411	5.419	5.447	5.489	5.528
c /Å	7.611	7.625	7.680	7.745	7.786
V /Å^3	221.17	222.32	226.97	232.93	236.83
c/√2 /Å	5.382	5.392	5.431	5.476	5.506
a, b, c/√2 relation	a<c/√2<b	a<c/√2<b	a<c/√2<b	c/√2≤a<b	a≤c/√2<b
a' /Å	3.810	3.816	3.843	3.876	3.897
α /%	0.292	0.266	0.158	0.086	0.194

rhomboherdal phase stability toward higher Fe content (x). On the contrary, in the $Pr_{1-y}Sr_yCo_{1-x}Fe_xO_{3-\delta}$ perovskite structure with larger Pr replace La the orthorhombic phase existence range in the first approximation are between x= 0.0 and x=1.0.

Apparently the orthorhombic structural relationship between lattice parameters of $Pr_{1-y}Sr_yCo_{1-x}Fe_xO_{3-\delta}$ solid solution is in seemingly agreement with those of Meng et al. [17] who recently found a single orthorhombic perovskite-structure ($PrCoO_3$-type) in the $Pr_{1-y}Sr_yCo_{0.8}Fe_{0.2}O_{3-\delta}$ solid solution when mole fraction of Sr was between 0.2 and 0.6, and with those of Qiu et al. [30] who resolved XRD patterns obtained in the $Pr_{1-y}Sr_yCo_{1-x}Fe_xO_{3-\delta}$ (y=0.2−0.3; $0.0 \leq x \leq 1.0$) as an orthoferrite structure ($GdFeO_3$-type) with space group *Pbnm*. While, it can be note that recently Kim and co-workers registered a small peak split at 59° (2θ) just for $Pr_{0.3}Sr_{0.7}Co_{0.7}Fe_{0.3}O_{3-\delta}$ samples [18].

These lattice parameters discrepancies result from the fact that the $Pr_{1-y}Sr_yCo_{1-x}Fe_xO_{3-\delta}$ solid solution phase does not take into account correlations existing between structure and oxygen content (δ). Comparing experimental data obtained from literature and discrepancies results we suggest that further studies are necessary to understand the structure behavior of $Pr_{1-y}Sr_yCo_{1-x}Fe_xO_{3-\delta}$ solid solution as a function of Sr- and Fe- content and mole fraction of oxygen content (δ). In fact, at present, a huge gap of knowledge is recorded on the crystal-structure behavior of the $Pr_{1-y}Sr_yCo_{1-x}Fe_xO_{3-\delta}$ system in terms of oxygen content (δ). Our observation is consistent with the findings by Kostogloudis et al., who suggested that the not-linear lattice expansion and Thermal Expansion Coefficient (TEC) behaviors observed at high temperatures in the $Pr_{1-y}Sr_yCoO_{3-\delta}$ oxides ($0.0 \leq x \leq 0.5$) may be attributed to a loss of lattice oxygen and the formation of oxygen vacancies [31].

Table 1 shows the relationship between the pseudocubic unit cell parameter (*a'*), defined as the cube root of the unit cell volume into ABO_3 unit (A = Pr, Sr; B = Co, Fe) and the type of orthorhombic structure, as a function of the Fe content (x), indicating the fields of the symmetry existence of $Pr_{0.8}Sr_{0.2}Co_{1-x}Fe_xO_{3-\delta}$ solid solutions. For the calcined powders, the lattice constants (*a, b, c*) and the cell volume (V) progressively increased, as well as the pseudocubic lattice parameter (*a'*), with increasing the Fe content (x). In particular, the pseudocubic lattice parameter increased almost linearly from ~3.81 to ~3.90 Å ($\Delta a' \cong +2.3\%$) with increasing the Fe content (x) from $Pr_{0.8}Sr_{0.2}CoO_{3-\delta}$ to $Pr_{0.8}Sr_{0.2}FeO_{3-\delta}$, respectively, in agreement with the Vegard's law. Moreover, the pseudo-cubic lattice constant behavior upon modification of Fe content (x) is in good agreement with experimental results by Tai et al. [2, 3] for the LSCF system, where lanthanum replaced praseodymium, and with structural results by Piao et al. [32]. Contrariwise, some authors suggested that the Vegard`s law deviation in lattice constant of $Pr_{1-y}Sr_yBO_{3-\delta}$ (B = Fe or Co) as a function of Sr content (y) is ascribed to the formation of oxygen vacancies [31].

The α orthorhombic distortion, as reported by Piao et al. [32], is an anisotropy parameter that indicates the distortion relative to the ideal perovskite structure. The values of α, calculated from each compound, are shown in Table 1. As can be found, the α value of x=0.0 was the highest because of the deviation values of cell parameters (a, b). The increase of Fe content (x) results in the decrease of α, which reaches smallest value at x=0.8. The α value increases again when x=1.0 because of the deviation of the lattice parameters.

3.4 Morphological analysis

From XRD patterns, the crystallite sizes were calculated using the Scherrer's equation for the as-combusted and calcined powders. For the as-combusted powders, the crystallite size did not change much with the Fe content (x). The crystallite size significantly increased, as expected, with the heating temperature from CS to 1273 K. Scherrer's results shows that the crystallite size for the as-combusted powders was in the 10–16 nm range, and increased up in the 75–90 nm range after heating. The increase in the crystallite size depended on the Fe content (x): for the pure cobaltite (x=0.0) the crystallite size increased slightly from 16 to 90 nm, while the crystallite size for the samples with x=1.0 was 75 nm. One can observe also that the crystallite size of the as-combusted powders was significantly smaller than their grain size observed by SEM. Figure 4 shows the representative SEM micrographs of the x=0.0 and x=1.0 nano-size powders heated to 1273 K. After thermal treatment, the particle size of the $Pr_{0.8}Sr_{0.2}Co_{1-x}Fe_xO_{3-\delta}$ oxides, calculated by the intercept method, grew up above ~150 nm, but the particle size of powders decreased as the Fe content (x) increased. The particle size parameters of $Pr_{0.8}Sr_{0.2}CoO_{3-\delta}$ samples (250 nm) are larger than that of the $x \geq 0.2$ samples (190–150 nm), as reported in Table 2.

3.5 Electrochemical characterization

As an example for all the electrode compositions, Fig. 5 shows the Nyquist plots measured using a two-probe configuration for $Pr_{0.8}Sr_{0.2}Co_{0.5}Fe_{0.5}O_{3-\delta}$ symmetrical electrodes on a doped-ceria electrolyte on the range of temperature studied. The inserts in Fig. 5 show the magnification of the high-frequency region. Figure 5(e) shows the EIS plot measured at 873 K. The electrical circuit used for fitting the EIS data is shown in insert of Fig. 5(f). Symbols R_{HF}, R_{MF} and R_{LF} describe resistance at high,

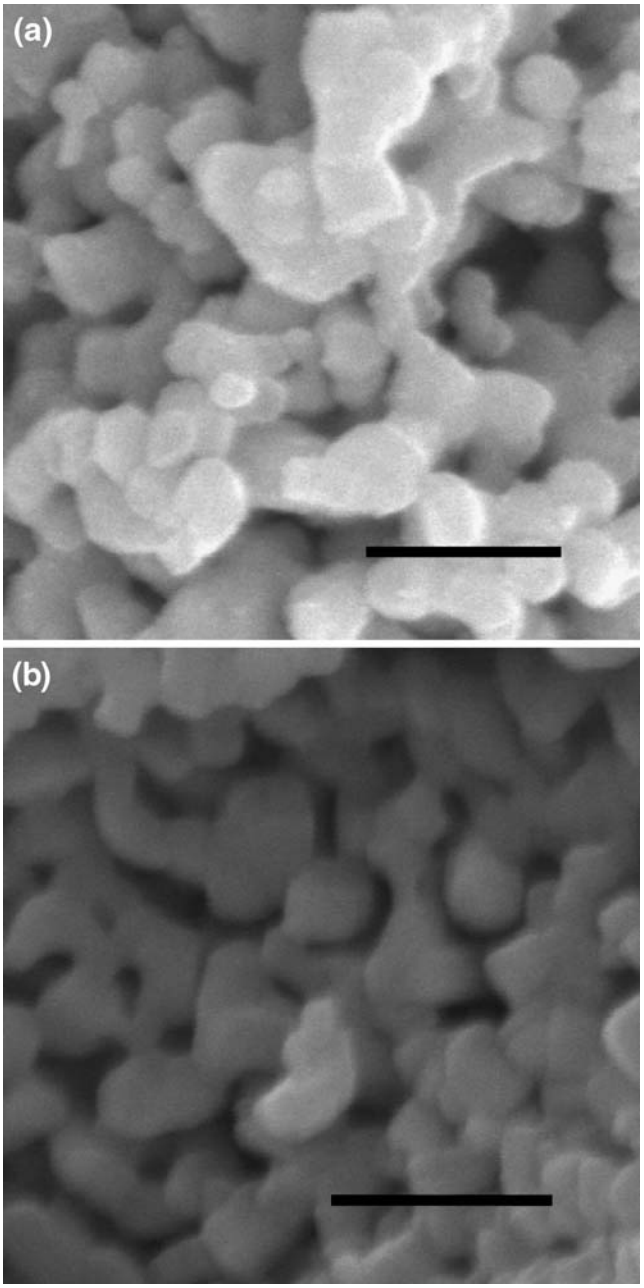

Fig. 4 Representative micrographs of (**a**) $Pr_{0.8}Sr_{0.2}CoO_{3-\delta}$ and (**b**) $Pr_{0.8}Sr_{0.2}FeO_{3-\delta}$ powders annealed at 1273 K for 2 h in air (black scale marker bars are 500 nm)

medium and low frequency, respectively; W accounts for a Warburg element, and CPE is the symbol for the constant phase element.

The EIS plots of the $Pr_{0.8}Sr_{0.2}Co_{0.5}Fe_{0.5}O_{3-\delta}$ samples clearly showed at least two semicircles. Each resistance can be assigned to the resistance associated with a specific electrochemical process and can be calculated by nonlinear least square fitting to experimental data. At 873 K, a semicircle at high frequency that did not intercept the origin was observed. This semicircle tended to collapse to a single point with increasing temperature. Reasonably, these features can be correlated to phenomena occurring at the electrolyte (called Process I, in Fig. 5(f)), being the intercept with the real axis at high frequency ascribable to the electrolyte resistance [33] and, which agree with those reported in previous works [34], the semicircle observed at low temperatures due to grain-boundary resistance [35].

At 873 K and low frequencies the presence of a line inclined at 45° followed by a semicircle was observed. With increasing temperature, the linear spur tended to transform into another semicircle. The sum of these processes can be correlated to the phenomena occurring at the electrode and electrode/electrolyte interface (called Process II, Fig. 5(f)). The 45° degree straight line behavior is characteristic of semi-infinite diffusion and was successfully fitted with a Warburg element [36]. EIS plots with similar shape were attributed to Gerischer impedance due to a co-limited reaction regime where both kinetics and transport determine the electrode characteristics [1]. However, in the present case modeling with Gerischer impedance did not satisfactorily fit the measured data [37]. Therefore, the linear spur was attributed to diffusion, which became favored with increasing temperature, transforming to finite diffusion semicircle. The final loop at the lowest frequencies can probably be attributed to charge transfer at the electrode/electrolyte interface. Therefore, the intercept with the real axis at the lowest frequencies can give the resistance for the oxygen electrode reaction. No polarization was observed at low frequencies, showing that the perovskite-type oxides possessed significant electronic conductivity.

Table 2 Some selected properties of $Pr_{0.8}Sr_{0.2}Co_{1-x}Fe_xO_{3-\delta}$ powders and electrode films.

Fe content (x)	Powder /nm	Electrode	
		Film tickness /μm	Powder grain size /nm
0.0	250	65	250
0.2	190	80	190
0.5	150	80	150
0.8	170	80	170
1.0	160	80	160

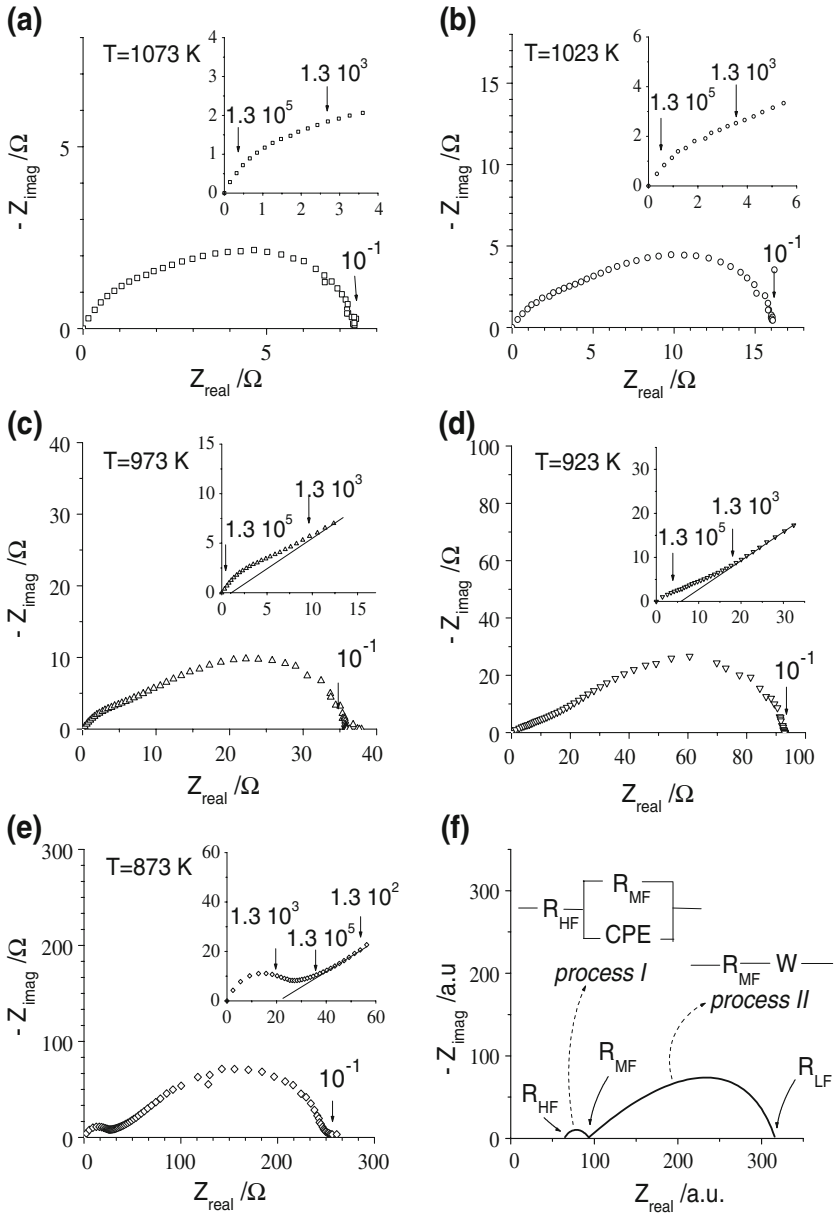

Fig. 5 EIS complex impedance plane plots recorded at (**a**) 1073, (**b**) 1023, (**c**) 973, (**d**) 923 and (**c**) 873 K in air for the $Pr_{0.8}Sr_{0.2}Co_{0.5}Fe_{0.5}O_{3-\delta}$ sample (x = 0.5). The high frequency part is enlarged in the insets. Tangential lines are a guide to the eyes. Fitting of the EIS plot measured at 873 K, with the equivalent circuit showing the two impedance elements associated with each semicircle (called Process I and II in f). With: R_{HF} = resistance at high-frequency, R_{MF} = resistance at medium-frequency, R_{LF} = resistance at low-frequency, CPE = constant phase element, and W = Warburg element

The EIS data were used to derive the area specific resistance (ASR) of the interface for nano-sized $Pr_{0.8}Sr_{0.2}Co_{1-x}Fe_xO_{3-\delta}$ electrodes and the Activation Energy (E_a) of the process to understand the effects of Fe composition (x) on the electrochemical properties [38].

Figure 6 show the temperature-dependence of the interface conductivity and ASR, respectively, for $Pr_{0.8}Sr_{0.2}Co_{1-x}Fe_xO_{3-\delta}$ solid solutions as a function of Fe content (x). With increasing the temperature, conductivity increased logarithmically, showing an Arrhenius-type temperature dependence. The solid lines in the Fig. 6 represent least square fits for the measured data.

The ASR was the smallest for the $Pr_{0.8}Sr_{0.2}Co_{0.2}Fe_{0.8}O_{3-\delta}$ sample (2.36 Ω cm^2 at 973 K). The ASR of $Pr_{0.8}Sr_{0.2}FeO_{3-\delta}$ (x=1.0) electrode was larger than that of the $Pr_{0.8}Sr_{0.2}Co_{0.5}Fe_{0.5}O_3$ (x=0.5) and $Pr_{0.8}Sr_{0.2}Co_{0.8}Fe_{0.2}O_{3-\delta}$ (x=0.2) electrodes but there was a different behavior on the $Pr_{0.8}Sr_{0.2}CoO_{3-\delta}$ electrode (x=0.0). These ASR performances make this material a promising potential candidate for SOFC applications as a future

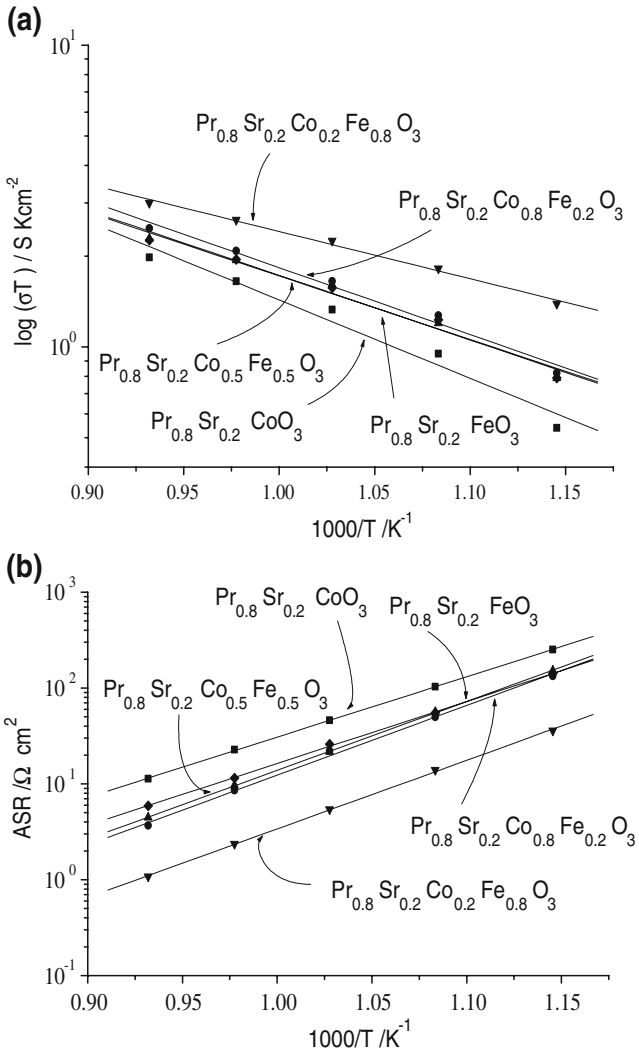

Fig. 6 (**a**) Arrhenius plots of electrode process, and (**b**) area specific resistance versus the reciprocal of temperature (solid lines guide the eye) for $Pr_{0.8}Sr_{0.2}Co_{1-x}Fe_xO_{3-\delta}$ nanocrystalline powders in symmetrical cells

composite cathode which can match well with SDC electrolyte.

The Activation Energy (E_a) for all the samples was calculated to be in the 1.33–1.52 eV range. More specifically the Ea (±0.02 eV) of the x=0.0, 0.2, 0.5, 0.8 and 1.0 samples in the $Pr_{0.8}Sr_{0.2}Co_{1-x}Fe_xO_{3-\delta}$ systems were 1.33, 1.52, 1.50, 1.50 and 1.36, respectively. The variation of E_a with composition differs from that of the ASR: the lowest E_a was observed for the $Pr_{0.8}Sr_{0.2}CoO_{3-\delta}$ (x=0.0) sample, which showed the largest ASR.

The activation energy values obtained in this work for $Pr_{0.8}Sr_{0.2}Co_{1-x}Fe_xO_{3-\delta}$ solid solutions are of the same order of magnitude as the E_a reported for LSCF electrode (1.60 eV) by Bae and Steele [39] and for Sr-Ce-Fe-Co-O system (1.44 eV) by Colomer et al. [40] on ceria electrolytes, suggesting that this electrode is compatible with cathode technology and is a potential candidate for the fabrication of SOFC, as recently reported by Meng and coworkers [17].

Moreover, we tried to evaluate separately the E_a for the ASR associated with Process I and with Process II. For the $Pr_{0.8}Sr_{0.2}Co_{0.5}Fe_{0.5}O_{3-\delta}$ samples, the activation energy related to Process I (i.e., associated with the electrolyte) was 0.83±0.02 eV, which is in agreement with E_a values reported in the literature for the conductivity of SDC [41]. Quite similar results are obtained with other electrodes [34], which confirm our experimental results.

For Process II (i.e., associated with the electrode) E_a was 1.48±0.02 eV, which was the same value measured for the E_a of ASR derived from total resistance. Apparently, this means that the rate determining process for the $Pr_{0.8}Sr_{0.2}Co_{1-x}Fe_xO_{3-\delta}$ electrodes is their surface reaction with gas. Therefore, the presence of a single slope indicates that the same reaction mechanism controls the overall electrode behavior in the temperature range studied.

Regarding electrochemistry behavior of $Pr_{0.8}Sr_{0.2}Co_{1-x}Fe_xO_{3-\delta}$ electrode, there are poor literature data about its ASR. Moreover, there is poor literature documentation on the mechanical properties of $Pr_{0.8}Sr_{0.2}Co_{1-x}Fe_xO_{3-\delta}$ cathode ceramics. In all case, we can be noted that Fe content (x) makes an important contribution to the electrochemical reaction. As examples, we noted that the substitution of Fe on the Co-site makes the overpotentials increase slightly in the composition range of 0.0 and 0.8 and drastically increase at x=1.0 content [30], as was also confirmed by Zhu et al. which reported a lower cathode overpotential curve at x=0.1 in the $Pr_{0.7}Sr_{0.3}Co_{1-x}Cu_xO_{3-\delta}$ cathode on the SDC disk [19]. If the cathode overpotential is closely related to a kinetics of oxygen exchange, diffusion in the cathode materials as well to as to the oxygen vacancy, we can be concluded that electrochemical performances are very closely related to a structure behaviors at high temperature and electrode morphology nature. At the same time, the TEC match between $Pr_{0.8}Sr_{0.2}Co_{1-x}Fe_xO_{3-\delta}$ electrode and electrolyte is very important point and in the first approximation depend on Fe content (x), oxygen vacancies and crystalline structure. Moreover, it is well known that in the $La_{0.8}Sr_{0.2}Co_{1-x}Fe_xO_{3-\delta}$ system the rhombohedra phase always exhibits a higher TEC than the orthorhombic symmetry and, simultaneously, that the oxygen deficiency structure is also enhanced at high temperature [2].

It can be note that the best electrochemical performances in the $Pr_{0.8}Sr_{0.2}Co_{1-x}Fe_xO_{3-\delta}$ correspond to orthorhombic-type structure electrodes with low α value (x=0.8) and the ASR was highest for the high-distorted $Pr_{0.8}Sr_{0.2}CoO_3$ phase (x=0.0). Thus, the lattice expansion of $Pr_{0.8}Sr_{0.2}Co_{1-x}Fe_xO_{3-\delta}$ phase system when x≤0.2, and attributed to a loss of lattice oxygen of high-distortion orthorhombic-type

structure, probably increases more rapidly than x=0.8 sample as a function of temperature (T<1073 K). The relationships between chemical composition and electrode film micrograph for $Pr_{0.8}Sr_{0.2}Co_{1-x}Fe_xO_{3-\delta}$ system are subjects of the next paragraphs, whereas the relationships between crystal structure at high-temperature and TEC as a function of oxygen content (δ) are subjects for future investigations.

The oxygen reduction reaction seems to control the $Pr_{0.8}Sr_{0.2}Co_{1-x}Fe_xO_{3-\delta}$ electrode performance. The kinetic parameters of this reaction are influenced by several factors, although the reaction of molecular oxygen with the $Ce_{0.8}Sm_{0.2}O_{2-\delta}$ electrolyte surface, at first instance, can be neglected because the surface exchange coefficient values at SDC/gas interface are very low at these temperatures [1].

To better understand the nature of the phenomena driving the rate determining step, it was decided to investigate the influence of the gas atmosphere and typical results are reported for $Pr_{0.8}Sr_{0.2}Co_{0.5}Fe_{0.5}O_{3-\delta}$ samples (x=0.5). Figure 7 shows the complex impedance plane plots for the $Pr_{0.8}Sr_{0.2}Co_{0.5}Fe_{0.5}O_{3-\delta}$ samples measured at 1073 K in air and in argon inert atmosphere, respectively. The resistance at low frequencies dramatically increased in argon. On the other hand, the intercept with the real axis at high frequencies slightly decreased in argon as compared to air. Once again these data confirmed that the rate determining process for $Pr_{0.8}Sr_{0.2}Co_{1-x}Fe_xO_{3-\delta}$ electrodes is the surface reaction with gas and the oxygen surface exchange process primarily dominates the oxygen reduction reactions between 873 and 1073 K. Moreover, we also noticed that the Process I located at the high frequency side remains almost unchanged with the change of the oxygen partial pressure. On the basis of these results, we concluded, as reported before, that the highest frequency process was attributed to interfacial electrochemical kinetics process at the SDC/$Pr_{0.8}Sr_{0.2}Co_{1-x}Fe_xO_{3-\delta}$ interface. The results

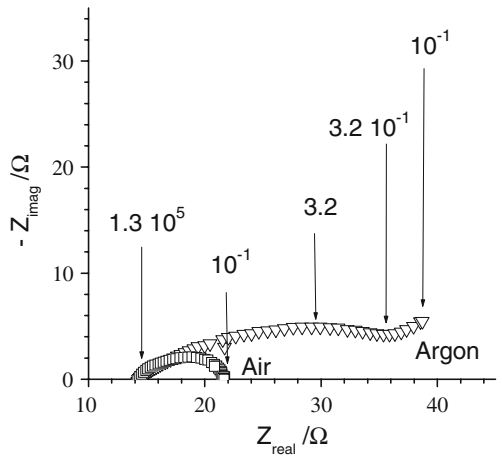

Fig. 7 EIS complex impedance plane plots of $Pr_{0.8}Sr_{0.2}Co_{0.5}Fe_{0.5}O_{3-\delta}$ electrodes measured in air or argon at 1073 K

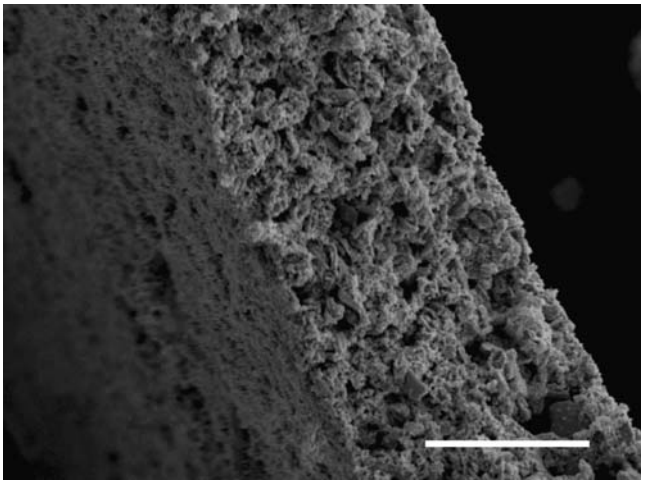

Fig. 8 A representative micrograph of $Pr_{0.8}Sr_{0.2}Co_{0.8}Fe_{0.2}O_{3-\delta}$ electrode layers (the scale marker bar is 50.0 μm)

reported in Fig. 7 show that the rate determining step of oxygen reduction is probably controlled by a surface exchange reaction that involves dissociative-adsorption reaction and diffusion of oxygen on the $Pr_{0.8}Sr_{0.2}Co_{1-x}Fe_xO_{3-\delta}$ electrode surface, and migration of oxygen ions from the electrode to the SDC electrolyte.

Moreover, the apparent E_a of the oxygen reduction reaction at $Pr_{0.8}Sr_{0.2}Co_{1-x}Fe_xO_{3-\delta}$ electrodes (Fig. 6) varied as a function of Fe content (x), indicating that the overall energy strongly depended on the nature and composition of the metal ions. However, also the particle size of the powders was affected by the same parameter. Therefore, it is necessary to understand whether the electrochemical properties are really affected by the chemical composition, the crystal structure or microstructural correlated with the Fe content (x). Thus, a detailed microstructural analysis on the electrodes was necessary to develop a better understanding of the correlation between electrochemical properties and Fe content (x).

Figure 8 shows the SEM micrographs of the typical cross-section of Pr-based cathodes prepared by heating the films at 1273 K. The cross-section photographs were obtained by observing mechanically fractured sample. As reported in Table 2, the film thickness was measured to be 80±5 μm for all the films (1.0≤x≤0.2), except for the pure cobaltite sample (x=0.0) that was measured to be 65±5 μm. The films obtained in this way were highly porous.

Figure 9 shows typical SEM micrographs of the surface of the $Pr_{0.8}Sr_{0.2}Co_{1-x}Fe_xO_{3-\delta}$ electrode films as a function of Fe content (x). It is possible to observe that the particle size distribution in the films was relatively narrow. As reported in Table 2, the average grain size of electrode films varied from 250 to 150 nm from $Pr_{0.8}Sr_{0.2}CoO_{3-\delta}$ to $Pr_{0.8}Sr_{0.2}FeO_{3-\delta}$, respectively. Moreover, from high magnification SEM micrographs of electrode films, it can also be

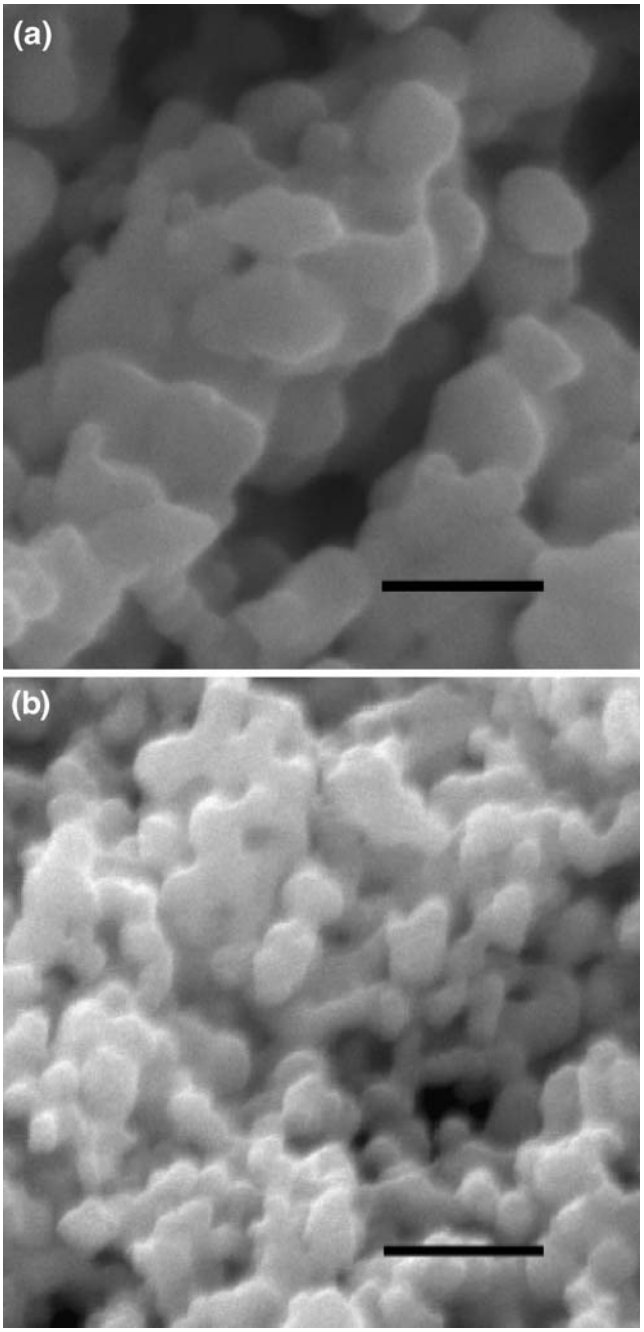

Fig. 9 Representative high magnification SEM images of of (**a**) $Pr_{0.8}Sr_{0.2}CoO_{3-\delta}$ and (**b**) $Pr_{0.8}Sr_{0.2}FeO_{3-\delta}$ electrode layers (black scale markers are 500 nm)

seen that the grain size is found to decrease with the film thickness. Further, particle size decreased with an increasing in Fe content (x) value, and partial agglomeration of these particles were observed at low Fe content (x). The well-developed crystalline particles with regular shape and high surface particle were observed for $x \geq 0.8$ electrode.

Another relevant fact related with cathode performance is the presence of surface cracks at low Fe content (x). Figure 10 shows the SEM micrographs of electrolyte films with different Fe content (x). The propagation of surface cracks has been observed in $Pr_{0.8}Sr_{0.2}CoO_{3-\delta}$ electrode, while big cracks have not been observed for the electrode films with $x \geq 0.2$ deposited by screen-printing. Consequently in order to explain the experimental results, it must be emphasized that the samples surface morphology shows a clear relation with the Fe content (x).

In the absence of Fe, for x=0.0 sample, the surface of the $Pr_{0.8}Sr_{0.2}CoO_{3-\delta}$ electrode (Fig. 10(a)) is seen to have a larger well-known crack size morphology, distributed between 5 and ~20 μm, and the electrode surface presents a rough shape. The result obtained from $Pr_{0.8}Sr_{0.2}CoO_{3-\delta}$ electrode surface is consistent with the findings by Grunbaum et al. who noted that the origin of these cracks may be related with differences in shrinkage during the heat treatment performed of green powder on the electrolyte surface [36]. A more compact structure is observed as the Fe content (x) from x=0.2 to x=1.0. More specifically, we can denote that the x=0.8 (Fig. 10(d)) and x=1.0 (Fig. 10(e)) electrode films are crack-free, while films of x=0.2 (Fig. 10(b)) and x=0.5 (Fig. 10(c)) present some very small surface cracks (<5 μm).

Another relevant experimental result related to surface of the $Pr_{0.8}Sr_{0.2}Co_{0.2}Fe_{0.8}O_{3-\delta}$ electrode. It can be seen that x=0.8 electrode surface has a relatively rich pinhole structure, in comparison with other samples, and the pore size mainly distributed in the range of 2–5 μm. This uniform surface layer, with rough shape and same well size-distributed pinhole, is supposed to form better interfacial contact between electrolyte and electrode, as a confirmed the electrochemical measurements (cf. Fig. 6(b)) where the x=0.8 samples is found to be the best ASR values in the $Pr_{0.8}Sr_{0.2}Co_{1-x}Fe_xO_{3-\delta}$ system. In addiction, for x=0.8 similar α trend were shown where the smallest values was found for $Pr_{0.8}Sr_{0.2}Co_{0.2}Fe_{0.8}O_{3-\delta}$ sample (Table 1).

In addition, it can be noted that thermal compatibility with electrodes was exhibited at $x \geq 0.8$ in $Pr_{0.8}Sr_{0.2}Co_{1-x}Fe_xO_{3-\delta}$ samples [30, 31]. On the other hand, if the crack may represent an area at which there are local stress and then probably reduced the effective contact area between the two layers, we can be concluded that, keeping the manufacturing method unaltered for all electrode, the contact resistance of charge transfer processes occurring at the current collector/$Pr_{0.8}Sr_{0.2}CoO_{3-\delta}$ or $Pr_{0.8}Sr_{0.2}CoO_{3-\delta}$/electrolyte interfaces will increase. The explanations are in line with previous experimental measurements by EIS (cf. Fig. 6(a)) but a further optimization of the deposition temperature conditions of cathode is necessary to overcome this problem.

We can conclude that the electrode performance of $Pr_{0.8}Sr_{0.2}Co_{1-x}Fe_xO_{3-\delta}$ is not only influenced by the Fe contents (x), and as consequence the crystalline structure, but also strongly depends on nano/microstructural features

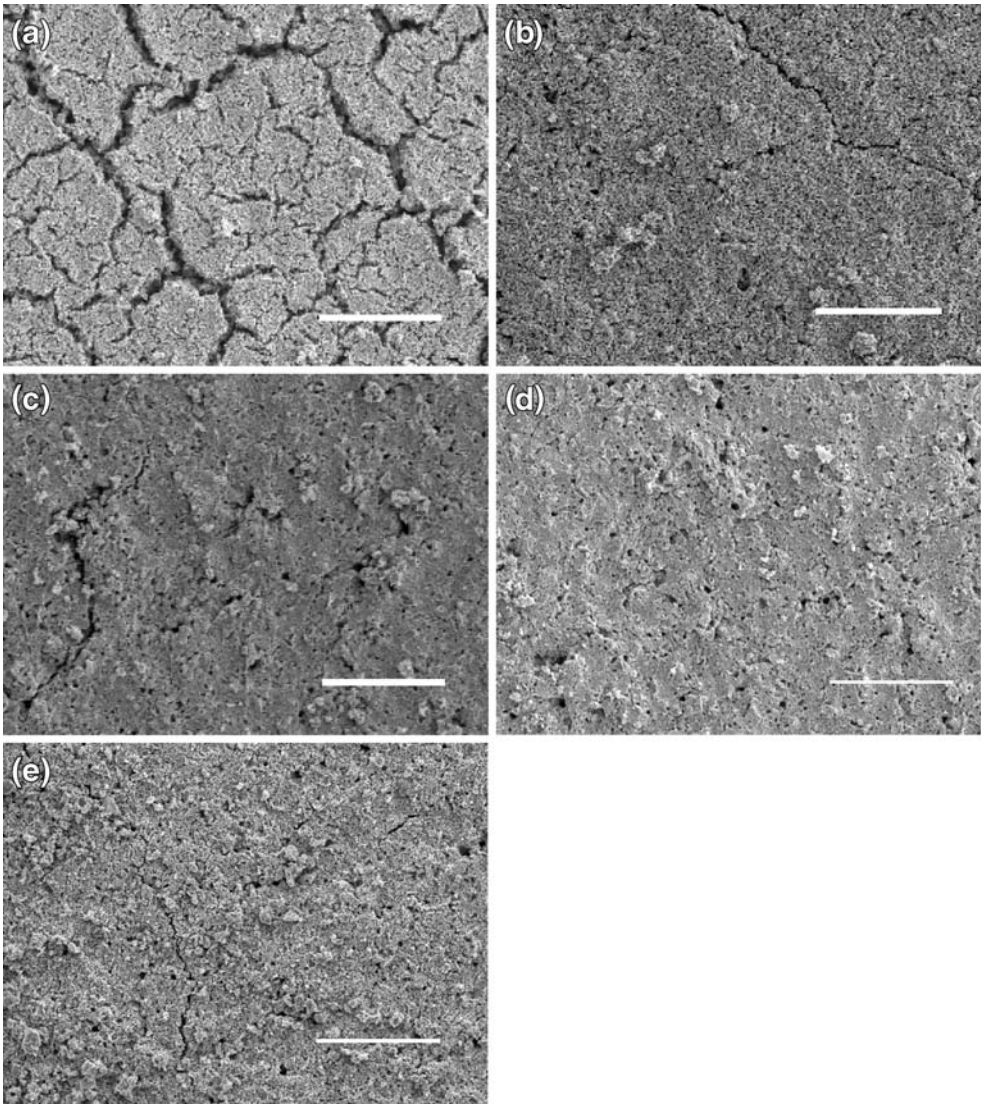

Fig. 10 Low magnification SEM images of representative $Pr_{0.8}Sr_{0.2}Co_{1-x}Fe_xO_{3-\delta}$ electrode layers: (**a**) x = 0.0, (**b**) x = 0.2, (**c**) x = 0.5, (**d**) x = 0.8 and (**e**) x = 1.0 (white scale marker bars are 100 μm)

of the material, notably the fired electrode morphological properties: both factors are to be considered together.

However, the possibility of starting the electrode fabrication from sub-micrometer powders could allow lowering the sintering temperature. Furthermore, $Pr_{0.8}Sr_{0.2}Co_{1-x}Fe_xO_{3-\delta}$ powders are a promising candidate for producing a composite cathode active material of SOFC. The test of these cathodes in an anode-supported fuel cell is planned in order to evaluate their performance under actual operating conditions.

4 Conclusions

In the present study, the crystal structure, morphological and electrochemical properties of $Pr_{0.8}Sr_{0.2}Co_{1-x}Fe_xO_{3-\delta}$ was investigated as a function of Fe content (x). $Pr_{0.8}Sr_{0.2}Co_{1-x}Fe_xO_{3-\delta}$ powders were prepared by the citrate-nitrate combustion synthesis than can produce final products without using any intermediate processes. Redox auto-combustion reaction between metal nitrate and citric acid yielded ultrafine $Pr_{0.8}Sr_{0.2}Co_{1-x}Fe_xO_{3-\delta}$ powders with average particle sizes on submicron level. This work has shown that CS process can be used with successful results to prepare $Pr_{0.8}Sr_{0.2}Co_{1-x}Fe_xO_{3-\delta}$ nano-powders suitable for SOFC cathode manufacturing.

All the compounds crystallize in a pure single phase perovskite-type and, moreover, the orthorhombic distortion symmetry α took place as a function of Fe content (x), which reaches smallest values at x=0.8.

The changes in microstructure of electrode film on SDC pellets were analyzed. The Fe content (x) has a crucial influence on the prepared powder characteristics and a significant influence on the electrochemical performance because the Fe content (x) has effects not only on the morphology of the cathode film during fabrications, but also on crystal structure and than on the surface exchange kinetics of electrocatalyst reactions.

The EIS data, measured as a function of the temperature, Fe content (x) and gas atmosphere clearly indicated that the resistance of symmetrical cells made with $Pr_{0.8}Sr_{0.2}Co_{1-x}Fe_xO_{3-\delta}$ electrodes originates mainly from low-frequency phenomena. The rate determining step was identified as the oxygen dissociative-adsorption and diffusion at $Pr_{0.8}Sr_{0.2}Co_{1-x}Fe_xO_{3-\delta}$ electrode surfaces and oxygen migration/diffusion between the SDC/$Pr_{0.8}Sr_{0.2}Co_{1-x}Fe_xO_{3-\delta}$ interfaces. In terms of electrochemical performance, the best composition was orthorhombic-type $Pr_{0.8}Sr_{0.2}Co_{0.2}Fe_{0.8}O_{3-\delta}$ (x=0.8) phase, which allowed obtaining an ASR value of 2.36 Ω cm^2, measured at 973 K.

Acknowledgments This work was partly supported by the Italian Ministry of Foreign Affairs (MAE) under the frame of the Italy-Japan joint lab on "Nanostructured Materials for Environment and Energy", by the Italian Ministry of University and Research (MiUR), under the frame of the FISR project "Polymer and Ceramic Electrolyte for Fuel Cells: System Validation and Development of New Materials", and by grants from "Japan Society for the Promotion of Science" (JSPS).

References

1. S.B. Adler, Chem. Rev. **104**, 4791 (2004). doi:10.1021/cr020724o
2. L.-W. Tai, M.M. Nasrallah, H.U. Anderson, D.M. Sparlin, S.R. Sehin, Solid State Ion. **76**, 259 (1995). doi:10.1016/0167-2738(94)00244-M
3. L.-W. Tai, M.M. Nasrallah, H.U. Anderson, D.M. Sparlin, S.R. Sehlin, Solid State Ion. **76**, 273 (1995). doi:10.1016/0167-2738(94)00245-N
4. M.M. Natile, E. Ugel, C. Maccato, A. Glisenti, Appl. Catal. Environ. **72**(3–4), 351 (2007). doi:10.1016/j.apcatb.2006.11.011
5. N.P. Bansal, Z. Zhong, J. Power Sources **158**, 148 (2006). doi:10.1016/j.jpowsour.2005.09.057
6. C. Peng, Z. Zhang, Ceram. Int. **33**(6), 1133 (2006). doi:10.1016/j.ceramint.2006.03.004
7. S.T. Aruna, M. Muthuraman, K.C. Patil, Solid State Ion. **111**(1–2), 45 (1998). doi:10.1016/S0167-2738(98)00187-8
8. L.A. Chick, L.R. Pederson, G.D. Maupin, J.L. Bates, L.E. Thomas, G.J. Exarhos, Mater. Lett. **10**(1–2), 6–12 (1990). doi:10.1016/0167-577X(90)90003-5
9. A. Mali, A. Ataie, Ceram. Int. **30**, 1979 (2004). doi:10.1016/j.ceramint.2003.12.178
10. A.S. Mukasyan, P. Epstein, P. Dinka, Proc. Combust. Inst. **31**, 1789 (2007). doi:10.1016/j.proci.2006.07.052
11. K.C. Patil, S.T. Aruna, S. Ekambaram, Curr. Opin. Solid State Mater. Sci **2**(2), 158 (1997). doi:10.1016/S1359-0286(97)80060-5
12. K.C. Patil, S.T. Aruna, T. Mimani, Curr. Opin. Solid State Mater. Sci. **6**(6), 507 (2002). doi:10.1016/S1359-0286(02)00123-7
13. M.S.G. Baythoun, F.R. Sale, J. Mater. Sci. **17**, 2757 (1982). doi:10.1007/BF00543914
14. D. Segal, J. Mater. Chem. **7**(8), 1297 (1997). doi:10.1039/a700881c
15. E. Magnone, E. Traversa, M. Miyayama, J. Ceram. Soc. Jpn. **115** (7), 402 (2007). doi:10.2109/jcersj.115.402
16. K. Shin-ichi, F. Arai, M. Ikezawa, J. Electron Spectrosc. Relat. Phenom. **78**, 135 (1996). doi:10.1016/S0368-2048(96)80045-4
17. X. Meng, S. Lu, Y. Ji, T. Wei, Y. Zhang, J. Power Sources **183**, 581 (2008). doi:10.1016/j.jpowsour.2008.05.052
18. J.H. Kim, S.-W. Baek, C. Lee, K. Park, J. Bae, Solid State Ion. **179**, 1490 (2008). doi:10.1016/j.ssi.2008.01.086
19. C. Zhu, X. Liu, D. Xu, D. Yan, D. Wang, W. Su, Solid State Ion. **179b**, 1470 (2008). doi:10.1016/j.ssi.2008.01.031
20. G.C. Kostogloudis, N. Vasilakos, C. Ftikos, J. Eur. Ceram. Soc. **17**, 1513 (1997). doi:10.1016/S0955-2219(97)00038-1
21. H.-R. Rim, S.-G. Jeung, E. Jung, J.-S. Lee, Mater. Chem. Phys. **52**, 54 (1998). doi:10.1016/S0254-0584(98)80006-0
22. V.N. Tikhonovich, V.V. Kharton, E.N. Naumovich, A.A. Savitsky, Solid State Ion. **106**, 197 (1998). doi:10.1016/S0167-2738(97)00505-5
23. G.C. Kostogloudis, C. Ftikos, Solid State Ion. **109**, 43 (1998). doi:10.1016/S0167-2738(98)00007-1
24. S.R. Jain, K.C. Adiga, V.R. Pai Verneker, Combust. Flame **40**, 71 (1981). doi:10.1016/0010-2180(81)90111-5
25. C. Julien, C. Letranchant, S. Rangan, M. Lemal, S. Ziolkiewicz, S. Catro-Garcia, L. El-Farh, M. Benkaddour, Mater. Sci. Eng. B **B76**, 145 (2000). doi:10.1016/S0921-5107(00)00431-1
26. Y.F. Zhang, J.X. Zhang, Q.M. Lu, Q.Y. Zhang, Mater. Lett. **60**, 2443 (2006). doi:10.1016/j.matlet.2006.01.013
27. Y.M. Hon, K.Z. Fung, M.H. Hon, J. Eur. Ceram. Soc. **21**, 515 (2001). doi:10.1016/S0955-2219(00)00217-X
28. U. Zavyalova, P. Scholz, B. Ondruschka, Appl. Catal. Gen. **323**, 226 (2007). doi:10.1016/j.apcata.2007.02.021
29. K. Deshpande, A. Mukasyan, A. Varma, J. Am. Ceram. Soc. **86** (7), 1149 (2003)
30. L. Qiu, T. Ichikawa, A. Hirano, N. Imanishi, Y. Takeda. Solid State Ion. **158**, 55 (2003). doi:10.1016/S0167-2738(02)00757-9
31. G.C. Kostogloudis, N. Vasilakos, C. Ftikos, Solid State Ion. **106**, 207 (1998). doi:10.1016/S0167-2738(97)00506-7
32. J. Piao, K. Sun, N. Zhang, X. Chen, S. Xu, D. Zhou, J. Power Sources **172**, 633 (2007). doi:10.1016/j.jpowsour.2007.05.023
33. E.P. Murray, T. Tsai, S.A. Barnett, Solid State Ion. **110**, 235 (1998). doi:10.1016/S0167-2738(98)00142-8
34. F. Mauvy, C. Lalanne, J.-M. Bassat, J.-C. Grenier, H. Zhao, L. Huo, P. Stevens, J. Electrochem. Soc. **153**(8), A1547 (2006). doi:10.1149/1.2207059
35. E.J.L. Schouler, N. Mesbahi, G. Vitter, Solid State Ionics **9 & 10**, 989 (1983)
36. N. Grunbaum, L. Dessemond, J. Fouletier, F. Prado, A. Caneiro, Solid State Ion. **177**, 907 (2006). doi:10.1016/j.ssi.2006.02.009
37. B.A. Boukamp, H.J.M. Bouwmeester, Solid State Ion. **157**, 29 (2003). doi:10.1016/S0167-2738(02)00185-6
38. D.P. Karim, A.T. Aldred, Phys. Rev. B **20**(6), 2255 (1979). doi:10.1103/PhysRevB.20.2255
39. J.M. Bae, B.C.H. Steele, J. Electroceram. **3**, 1 (1999). doi:10.1023/A:1009962831952
40. M.T. Colomer, B.C.H. Steele, J.A. Kilner, Solid State Ion. **147**, 41 (2002). doi:10.1016/S0167-2738(02)00002-4
41. Z. Zhan, T.-L. Wen, H. Tu, Z.-Y. Lu, J. Electrochem. Soc. **148**(5), A427 (2001). doi:10.1149/1.1359198